metrology

MDPI

Communication

Interferometric Surface Profile Measurement Based on Radial Polarization and Wavelength Variation

Yen-Chang Chu [1], Wei-En Bi [2], Jing-Heng Chen [1] and Kun-Huang Chen [2,*]

[1] Department of Photonics, Feng Chia University, Taichung 40724, Taiwan; ycchu@fcu.edu.tw (Y.-C.C.); jhchen@fcu.edu.tw (J.-H.C.)
[2] Department of Electrical Engineering, Feng Chia University, Taichung 40724, Taiwan; chenkht93016@gmail.com
* Correspondence: chenkh@fcu.edu.tw

Abstract

A radial-polarization-based interferometric method is proposed for measuring object surface profiles. In the proposed approach, a radially polarized beam is generated by transmitting a linearly polarized beam through a zero-order vortex half-wave plate and is then introduced into a modified Twyman–Green interferometer, in which the test specimen is placed in one interferometric arm. By introducing a small variation in the wavelength illumination, two interferometric intensity patterns are recorded using a CMOS camera. The corresponding phase difference distribution is retrieved from the recorded intensities and subsequently used to reconstruct the surface profile of the specimen. The feasibility of the proposed method is experimentally validated by measuring a standard gauge block, and the results show good agreement with theoretical predictions. Owing to its simple optical configuration, ease of alignment, high measurement accuracy, and rapid measurement capability, the proposed method demonstrates strong potential for practical surface profile measurement applications.

Keywords: radial polarized beam; surface profile measurement; dual-wavelength measurement technique

1. Introduction

In precision manufacturing and engineering applications, surface profile measurement plays a crucial role in quality control and performance evaluation and is widely used in industrial processes, precision components, and biomedical engineering. Therefore, the development of measurement techniques with both high accuracy and high efficiency is of great importance. Existing surface profilometry methods can be broadly classified into contact and non-contact approaches. Contact probe techniques can be applied to the surface profilometry of workpieces and thin films [1,2]. These methods acquire surface topography through mechanical scanning and offer structural simplicity; however, non-contact methods are generally more suitable for delicate or high-precision samples. Optical probe techniques can be applied to the surface profilometry of material cutting, modern circulated coins, and mirrors [3–6]. By replacing mechanical probes with laser scanning and intensity detection, these methods eliminate physical contact and reduce the risk of sample damage. Nevertheless, three-dimensional measurements typically require point-by-point scanning, which may limit measurement speed.

Interferometric techniques have been widely adopted due to their non-contact operation, full-field capability, and high resolution and have been extensively applied in the

Check for updates

Academic Editors: Steve Vanlanduit and Yuanchen Zeng

Received: 23 March 2026
Revised: 30 April 2026
Accepted: 1 May 2026
Published: 4 May 2026

Copyright: © 2026 by the authors. Licensee MDPI, Basel, Switzerland. This article is an open access article distributed under the terms and conditions of the Creative Commons Attribution (CC BY) license.

measurement of distance, surface roughness, and refractive index [7–10]. Various techniques have been developed in conventional interferometry for the analysis of measured objects. Single-wavelength interferometers are limited in measurement range by the optical wavelength, whereas dual-wavelength techniques [11–13] extend the measurable range and enhance phase unwrapping capability using a synthetic wavelength. White-light interferometry [14,15] further enables absolute height determination by exploiting low-coherence characteristics. In addition, fringe projection [16–19] and Moiré interferometry [20–23] are commonly employed for three-dimensional surface reconstruction and can be combined with heterodyne techniques to improve measurement stability [24].

In recent years, structured light generated through the modulation of different degrees of freedom has attracted considerable attention in optical analysis [25–27]. These degrees of freedom include the wavelength/frequency domain, which is associated with dispersion characteristics, and the time domain, which involves pulse properties such as delay and chirp. Furthermore, modulation of the amplitude and phase of the optical field introduces additional degrees of freedom, encompassing parameters such as the wave vector, wavefront, and transverse spin. In the polarization domain, further degrees of freedom can be exploited, including longitudinal spin, cylindrical vector beams, and vortex beams. Such structured light fields have been widely applied in various optical applications, such as optical trapping, surface plasmon excitation, high-resolution microscopy, laser machining, high-density data storage, and quantum information processing [28–32]. Among these, cylindrical vector beams are generated by tailoring the polarization state of light and exhibit axial polarization symmetry [32]. The spatially variant polarization distribution across the beam cross-section provides new opportunities for precise and real-time measurements. In many optical metrology techniques, the vectorial nature of the polarization field plays a crucial role. Radially polarized cylindrical vector beams exhibit polarization symmetry that enhances the signal-to-noise ratio in spatial resolution and enables sub-micrometer scale measurement capability [33]. A radial polarization interferometer is therefore demonstrated to achieve improved phase sensitivity compared with a conventional interferometer. In this configuration, the phase difference between the interferometer arms is encoded as a spatially varying intensity distribution through the interference of radially polarized beam.

Based on these developments, this study proposes a cylindrical vector beam interferometric profilometry method. A radially polarized cylindrical vector beam is employed as the illumination source, taking advantage of its axisymmetric polarization distribution. The system is implemented using a Twyman–Green interferometer [34,35] by modifying the configuration integrated with a dual-wavelength technique to establish a compact and rapid surface profilometry system. Only two interferograms are required to complete phase retrieval and surface reconstruction. Experimental validation using a standard gauge block demonstrates a system resolution of 61.42 μm, with a measurable range extended to the centimeter scale. The proposed method provides non-destructive, full-field, and rapid measurement capabilities with a relatively simple and cost-effective configuration.

2. Principles and Experimental Setup

Figure 1 schematically depicts the experimental configuration employed in this study. For clarity, the positive z-axis is defined along the direction of light propagation, while the x-axis is oriented perpendicular to the plane of the paper. A linearly polarized laser beam with wavelength λ, whose polarization direction is oriented at 90° with respect to the x-axis by using a polarizer (P), is expanded and collimated by a beam expander (BE). Subsequently, the linearly polarized beam is transformed into a radially polarized

symmetric beam using a radial polarized conversion element (Cr). The corresponding Jones vector can be expressed as

$$\begin{aligned} E_{in}(x,y) &= C_r \cdot E_{90^\circ} \\ &= \begin{bmatrix} -\sin\theta & \cos\theta \\ \cos\theta & \sin\theta \end{bmatrix} \cdot \begin{bmatrix} 0 \\ 1 \end{bmatrix} e^{i\omega_0 t} = \begin{bmatrix} \cos\theta \\ \sin\theta \end{bmatrix} e^{i\omega_0 t}, \end{aligned} \tag{1}$$

where ω_0 denotes the angular frequency of the light source, and θ represents the azimuthal angle at a given position in the beam cross section. The radially polarized beam is then divided into transmitted and reflected components by a beam splitter (BS). The transmitted beam is normally incident on the test specimen and is reflected back along its original optical path. The associated Jones vector is given by

$$\begin{aligned} E_t(x,y) &= BS_r \cdot S \cdot BS_t \cdot E_{in} \\ &= \tfrac{1}{\sqrt{2}} \begin{bmatrix} -1 & 0 \\ 0 & 1 \end{bmatrix} \cdot \begin{bmatrix} -e^{i\varphi(x,y)} & 0 \\ 0 & e^{i\varphi(x,y)} \end{bmatrix} \cdot \tfrac{1}{\sqrt{2}} \begin{bmatrix} 1 & 0 \\ 0 & 1 \end{bmatrix} \cdot \begin{bmatrix} \cos\theta \\ \sin\theta \end{bmatrix} e^{i\omega_0 t} \\ &= \tfrac{e^{i\varphi(x,y)}}{2} \begin{bmatrix} \cos\theta \\ \sin\theta \end{bmatrix} e^{i\omega_0 t}, \end{aligned} \tag{2}$$

where $\phi(x, y)$ represents the phase difference distribution introduced by the specimen. Meanwhile, the reflected beam is directed toward a mirror (M) and retraces its original path after reflection. Its Jones vector can be written as

$$\begin{aligned} E_r(x,y) &= BS_t \cdot M \cdot BS_r \cdot E_{in} \\ &= \tfrac{1}{\sqrt{2}} \begin{bmatrix} 1 & 0 \\ 0 & 1 \end{bmatrix} \cdot \begin{bmatrix} -1 & 0 \\ 0 & 1 \end{bmatrix} \cdot \tfrac{1}{\sqrt{2}} \begin{bmatrix} -1 & 0 \\ 0 & 1 \end{bmatrix} \cdot \begin{bmatrix} \cos\theta \\ \sin\theta \end{bmatrix} e^{i\omega_0 t} \\ &= \tfrac{1}{2} \begin{bmatrix} \cos\theta \\ \sin\theta \end{bmatrix} e^{i\omega_0 t}. \end{aligned} \tag{3}$$

The two beams are recombined at the BS and subsequently detected by a CMOS camera. The resulting Jones vector at the CMOS plane is therefore expressed as

$$\begin{aligned} E(x,y) &= (E_r(x,y) + E_t(x,y)) \\ &= \tfrac{1+e^{i\phi(x,y)}}{2} \begin{bmatrix} \cos\theta \\ \sin\theta \end{bmatrix} e^{i\omega_0 t}. \end{aligned} \tag{4}$$

Accordingly, the intensity recorded by the CMOS camera can be derived as

$$I(x,y) = |E(x,y)|^2 = \frac{1+\cos\phi(x,y)}{2}. \tag{5}$$

From Equation (5), the phase difference distribution $\phi(x, y)$ can be retrieved as

$$\varphi(x,y) = \cos^{-1}(2I(x,y) - 1). \tag{6}$$

Since the phase difference induced by the specimen is related to its surface height distribution by $\phi(x, y) = 4\pi D(x, y)/\lambda$, Equation (6) can be further rewritten as

$$D(x,y) = \frac{\lambda}{4\pi} \cos^{-1}(2I(x,y) - 1). \tag{7}$$

where $D(x, y)$ denotes the surface height distribution of the specimen. To extend the unambiguous measurement range, the illumination wavelength is changed to λ', leading to a modified phase difference distribution

$$\varphi'(x,y) = \cos^{-1}(2I'(x,y) - 1). \tag{8}$$

The resulting phase difference variation can therefore be expressed as

$$\begin{aligned} \Delta\varphi(x,y) &= \varphi(x,y) - \varphi'(x,y) \\ &= \cos^{-1}[2I(x,y) - 1] - \cos^{-1}[2I'(x,y) - 1]. \end{aligned} \tag{9}$$

This phase variation can also be represented in terms of an equivalent wavelength Λ as

$$\Delta\varphi(x,y) = 4\pi D(x,y)\frac{1}{\Lambda}, \tag{10}$$

where $\Lambda = \frac{\lambda\lambda'}{|\Delta\lambda|}$. Consequently, the surface height distribution $D(x, y)$ of the specimen can be determined as

$$D(x,y) = \frac{\Lambda}{4\pi}\left\{\cos^{-1}[2I(x,y) - 1] - \cos^{-1}\left[2I'(x,y) - 1\right]\right\}. \tag{11}$$

As indicated by Equation (11), accurate measurements of the intensities I and I' enable quantitative retrieval of the specimen surface height. By applying this procedure to each pixel of the CMOS image, the full surface profile of the tested object can be reconstructed.

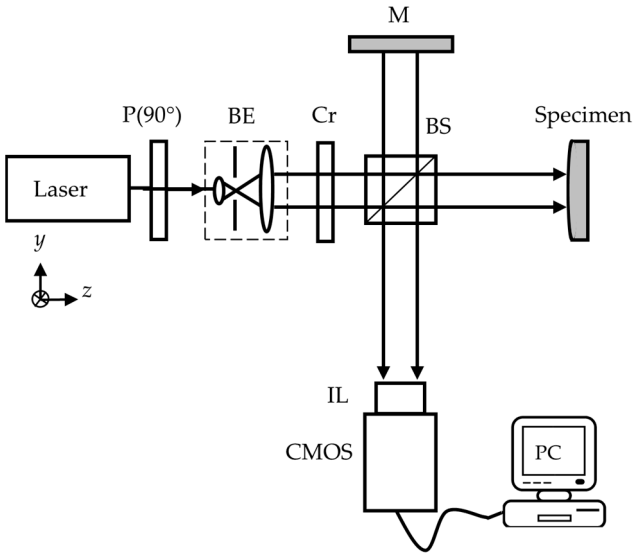


Figure 1. The experimental setup of the proposed method.

3. Experiments and Results

To assess the feasibility of the proposed method, the first to fifth steps of a standard step gauge were measured, and the specifications are shown in Figure 2. The experimental system consisted of a tunable diode laser (Model 6304, New Focus, Santa Clara, CA, USA) operating at wavelengths of λ = 632.8 nm and λ' = 632.82 nm, corresponding to a wavelength difference of $\Delta\lambda$ = 0.02 nm. The optical configuration further included a beam expander equipped with a 40× objective, a 5 µm pinhole, an achromatic lens with a focal length of 70 mm, and a zero-order vortex half-wave plate (Cr, WPV10L-633, Thorlabs, Newton, NJ, USA). The interference patterns were recorded using a CMOS camera (Basler A504k, Basler AG, Ahrensburg, Schleswig-Holstein, Germany) with an 8-bit gray level

and a spatial resolution of 1280 × 1024 pixels. All captured images were processed and analyzed using MATLAB (R2022b version) on a personal computer.

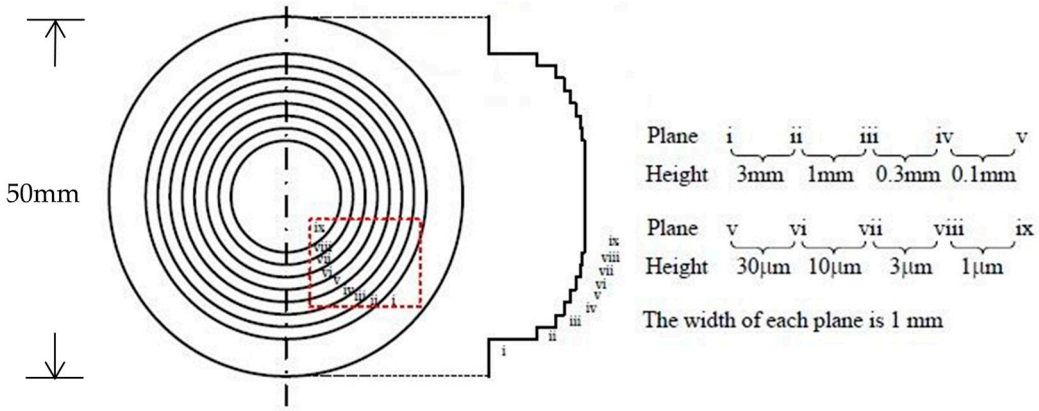
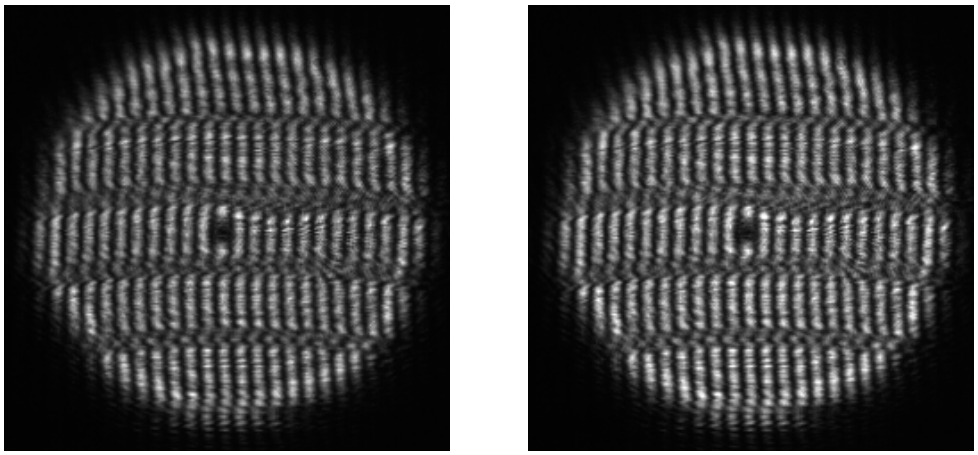


Figure 2. Schematic diagram of the standard step gauge specifications.

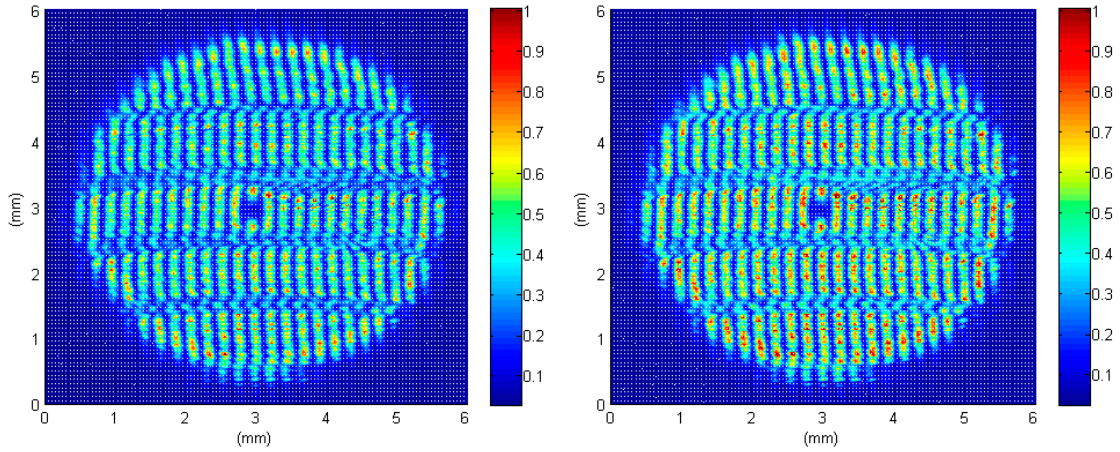
The interference patterns captured at wavelengths of 632.8 nm and 632.82 nm are shown in Figure 3. For computational convenience, the recorded interferograms were normalized in intensity using a MATLAB program, as illustrated in Figure 4. Subsequently, Equation (9) was employed to convert the normalized intensity distribution into a three-dimensional phase distribution, as shown in Figure 5, where the phase values range from 15° to 45°. Finally, the surface profile of the standard step gauge was reconstructed using Equations (10) and (11), and the resulting contour map is presented in Figure 6.



(**a**) (**b**)

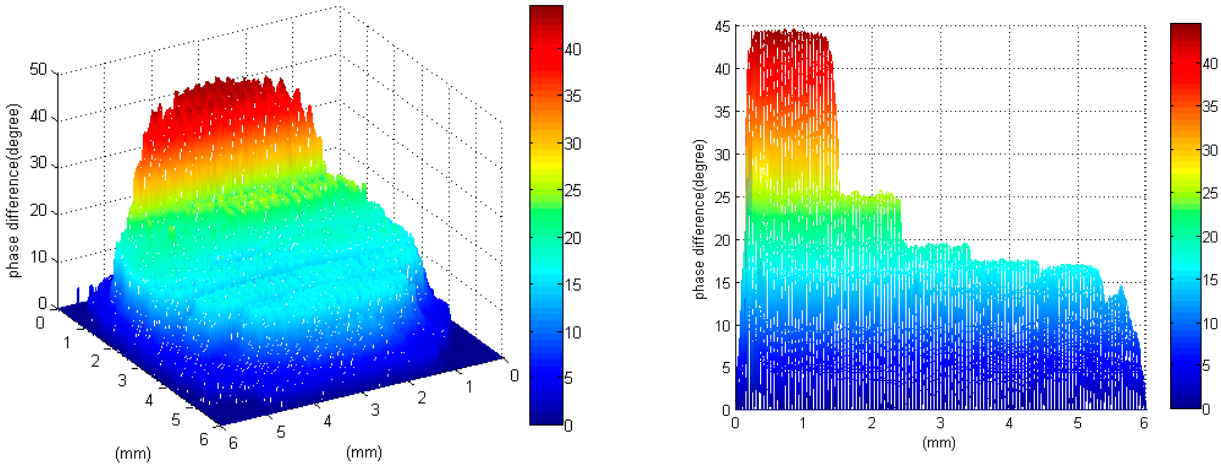
Figure 3. The results of two interferometric images for different wavelengths; (**a**) the wavelength at 632.8 nm and (**b**) the wavelength at 632.82 nm.

The reconstructed data for each step were averaged to obtain the recovered step heights of layers i–v, which are 6.96 mm, 3.95 mm, 3.07 mm, 2.80 mm, and 2.71 mm, respectively. The corresponding step height differences between adjacent layers were i−ii = 3.01 mm, ii−iii = 0.88 mm, iii−iv = 0.27 mm, and iv−v = 0.09 mm. These results are summarized in Table 1. As shown in Table 1, the experimental step height difference between steps ii and iii exhibits a relatively large absolute error of approximately 0.12 mm. This discrepancy is mainly attributed to the weak intensity near the center of the radially polarized vector beam. If this low-intensity region is excluded from the calculation, the absolute error can be effectively reduced to approximately 0.01 mm. Overall, the reconstructed values show good agreement with the reference values, thereby demonstrating the feasibility of the proposed method.



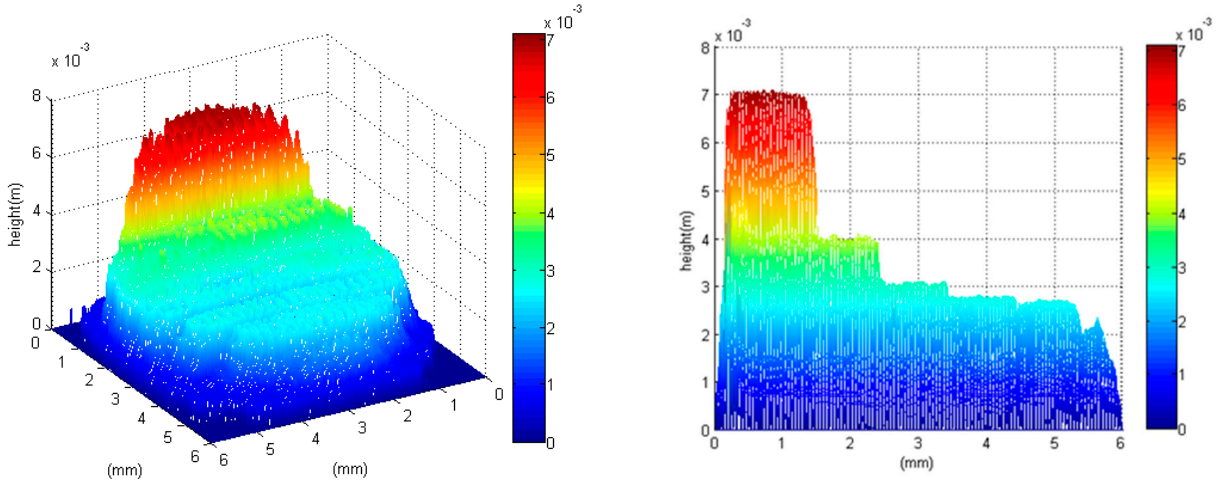
(**a**) (**b**)

Figure 4. The results of normalizing Figure 2; (**a**) the wavelength at 632.8 nm and (**b**) the wavelength at 632.82 nm.



(**a**) (**b**)

Figure 5. The results of the phase distribution of the surface of the standard step gauge: (**a**) three-dimensional view; (**b**) side view.



(**a**) (**b**)

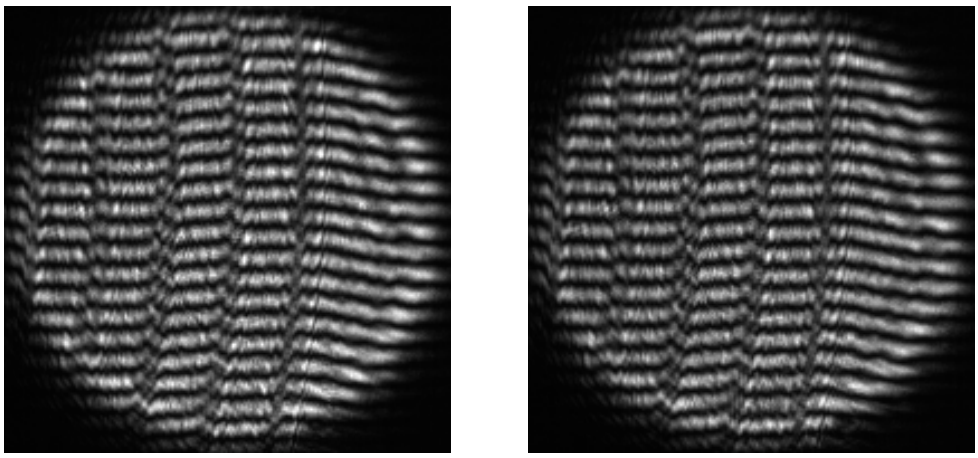
Figure 6. The results of the surface profile of the standard step gauge: (**a**) three-dimensional view; (**b**) side view.

Table 1. Summary of experimental data.

Step Height	Average Experimental Value	Step Height Difference	Experimental Values	Standard Value	Absolute Error
i	6.96 mm	i–ii	3.01 mm	3 mm	0.01 mm
ii	3.95 mm	ii–iii	0.88 mm	1 mm	0.12 mm
iii	3.07 mm	iii–iv	0.27 mm	0.3 mm	0.03 mm
iv	2.80 mm	iv–v	0.09 mm	0.1 mm	0.01 mm
v	2.71 mm				

4. Discussion

The optical configuration of the radially polarized interferometer (RPI) is more complex than that of conventional interferometry (CI), as it requires a zero-order vortex half-wave plate to generate a radially polarized beam. However, this configuration provides enhanced fringe contrast and higher spatial resolution. Figures 7 and 8 show the experimental results of surface profile reconstruction of a gauge block using CI. Figure 7 shows the interference patterns captured at wavelengths of 632.8 nm and 632.82 nm. Figure 8 shows the results of the surface profile of the standard step gauge. Based on Figures 3 and 6 of the RPI data compared with Figures 7 and 8 of the CI data, it can be concluded that the RPI fringes exhibit higher contrast and better resolution of height compared to those of CI. This enhanced spatial variation in the intensity distribution improves the robustness against the accuracy limitations imposed by the finite bit-depth quantization of the CCD camera used to record the interferograms.



(**a**) (**b**)

Figure 7. The results of two interferometric images for different wavelengths by using conventional interferometry; (**a**) the wavelength at 632.8 nm and (**b**) the wavelength at 632.82 nm.

In addition, for computational convenience, the intensity of recorded interferograms was normalized. The general intensity of interference can be written as

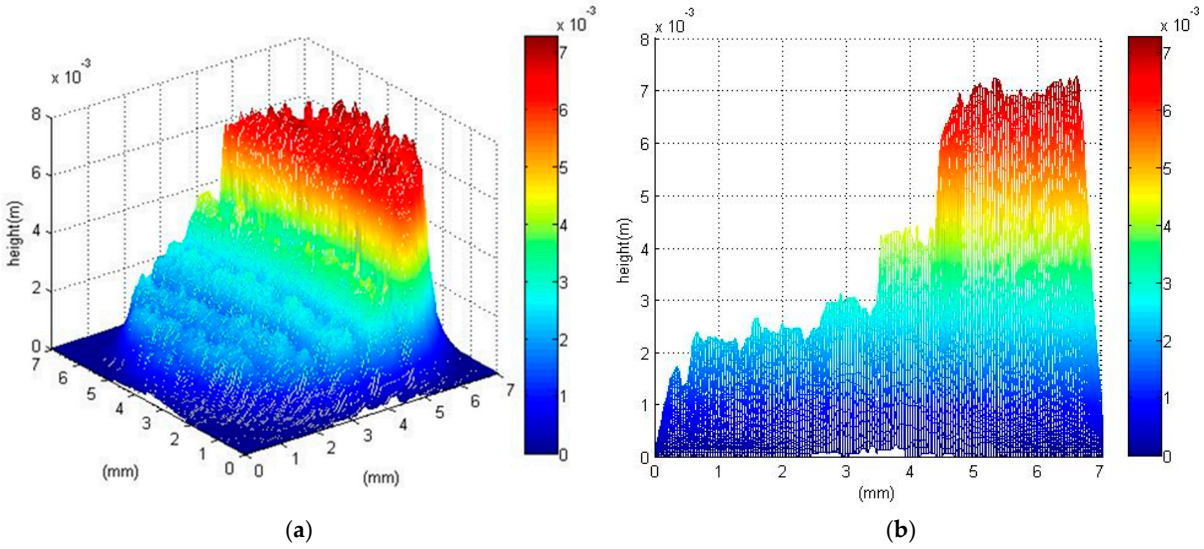
$$I(x,y) = I_0(x,y)(1+\cos\phi(x,y)), \tag{12}$$

where $I_0(x, y)$ represents bias intensity. In conventional interferometry, phase shifting is a famous method to eliminate bias intensity $I_0(x, y)$ and obtain the phase difference $\phi(x, y)$, but it could introduce more disturbances by mechanical phase shifting. In this study, the interference fringes captured by a CMOS camera are first normalized prior to phase analysis. The purpose of normalizing the fringe intensity is to eliminate the effects of

background intensity (bias/DC term), non-uniform illumination, and system responses, thereby ensuring that the resulting intensity depends solely on the phase term $\phi(x, y)$. The normalization procedure adopted in this work is expressed as follows:

$$I_{norm}(x,y) = \frac{I(x,y) - I_{min}(x,y)}{I_{Max}(x,y) - I_{min}(x,y)}, \tag{13}$$

where $I_{Max}(x, y)$ and $I_{min}(x, y)$ are the maximum and the minimum intensity in this experimental setup, respectively. Based on this formulation, the phase distribution $\phi(x, y)$ can be readily retrieved through normalization using MATLAB.



(**a**) (**b**)

Figure 8. The results of the surface profile of the standard step gauge by using conventional interferometry: (**a**) three-dimensional view; (**b**) side view.

According to Equation (11), the height measurement resolution ΔD_{err} associated with the proposed method can be expressed as

$$\Delta D_{err} = \left|\frac{\partial D}{\partial I} \cdot \Delta I_{err}\right| + \left|\frac{\partial D}{\partial I'} \cdot \Delta I'_{err}\right| + \left|\frac{\partial D}{\partial \lambda} \cdot \Delta \lambda_{err}\right| + \left|\frac{\partial D}{\partial \lambda'} \cdot \Delta \lambda'_{err}\right|, \tag{14}$$

where ΔI_{err} and $\Delta I^{'}_{err}$ denote the intensity errors of the CMOS camera, and $\Delta \lambda_{err}$ and $\Delta \lambda^{'}_{err}$ represent the wavelength uncertainties of the tunable laser source. Considering the intensity resolution of the CMOS camera, the values of ΔI_{err} and $\Delta I^{'}_{err}$ were estimated to be 0.0039. In addition, based on the wavelength resolution of the tunable diode laser (Model 6304, *New Focus*), both $\Delta \lambda_{err}$ and $\Delta \lambda^{'}_{err}$ were determined to be 0.02 nm. Substituting these parameters into Equation (14) yields a height resolution ΔD_{err} of approximately 61.42 μm. To further reduce the measurement uncertainty, a CMOS camera with a 16-bit gray level was employed. Under the same experimental conditions, the corresponding height resolution was reduced to 36.62 μm. This error analysis confirms that the proposed method provides high measurement accuracy and enhanced resolution.

5. Conclusions

A dual-wavelength cylindrical vector beam interferometric profilometry method has been demonstrated. By employing a radially polarized beam within a modified Twyman–Green interferometer, the proposed system enables phase retrieval and surface reconstruction using only two interferograms, significantly reducing measurement complexity and acquisition time. The use of radial-polarization beams enhances fringe contrast

and improves phase sensitivity, leading to robust performance under limited detector resolution. The feasibility of the proposed approach was experimentally verified by measuring a standard gauge block, resulting in a height measurement resolution of approximately 61.42 μm. Furthermore, the measurement accuracy can be improved by increasing detector bit depth, highlighting the scalability of the approach. The proposed technique provides a non-contact, full-field, and rapid surface measurement solution with a relatively simple and cost-effective configuration. It shows strong potential for applications in precision engineering, industrial inspection, and optical metrology, particularly in scenarios requiring large measurement ranges and high measurement efficiency.

Author Contributions: Conceptualization, Y.-C.C., K.-H.C., Data curation, W.-E.B.; Investigation, W.-E.B.; Methodology, K.-H.C., W.-E.B.; Writing—original draft, K.-H.C.; Writing—review and editing, Y.-C.C., J.-H.C. All authors have read and agreed to the published version of the manuscript.

Funding: National Science Council of the Republic of China, Taiwan (Nos. 114-2221-E-035-012 and 114-2221-E-035-013-MY2).

Data Availability Statement: Data underlying the results presented in this paper are not publicly available at this time but may be obtained from the authors upon reasonable request.

Conflicts of Interest: The authors declare no conflicts of interest.

References

1. Yu, B.; Ru, Q.; Sun, A.; Han, R.B.; Qu, K.; Ju, B.F. A contact probe based on multi-focus spectral confocal method for in-site measurement of form and position errors of complex surface workpieces. *Rev. Sci. Instrum.* **2025**, *96*, 035005. [CrossRef] [PubMed]
2. Park, J.; Cho, Y.J.; Chegal, W.; Lee, J.; Jang, Y.S.; Jin, J. A review of thin-film thickness measurements using optical methods. *Int. J. Precis. Eng. Manuf.* **2024**, *25*, 1725–1737. [CrossRef]
3. Ružbarský, J. Roughness Control of Surfaces Using a Laser Profilometer with the Selected Material Cutting Technology. *Materials* **2023**, *31*, 4109. [CrossRef]
4. Kapłonek, W.; Mikolajczyk, T.; Pimenov, D.Y.; Gupta, M.K.; Mia, M.; Sharma, S.; Patra, K.; Sutowska, M. High-Accuracy 3D Optical Profilometry for Analysis of Surface Condition of Modern Circulated Coins. *Materials* **2020**, *13*, 5371. [CrossRef]
5. Huang, P.S.; Xu, X.R. Design of an optical probe for surface profile measurement. *Opt. Eng.* **1999**, *38*, 1223–1228. [CrossRef]
6. Sugawara, H.; Yanagihara, M.; Asaoka, S.; Okusawa, M.; Maezaws, H. Development and performance of a profilometer for measurement of mirror surface figure. *J. Electron Spectrosc. Relat. Phenom.* **1996**, *80*, 485–488. [CrossRef]
7. Wang, D.; Ma, D.; Li, K.; Zhang, Y.; Zhao, J.; Wang, Y.; Rong, L. Dynamic full-field refractive index distribution measurements using total internal reflection terahertz digital holography. *Photon. Res.* **2022**, *10*, 289–296. [CrossRef]
8. Tsai, H.H.; Tsai, Y.J.; Lee, J.Y.; Cao, T.H. One-shot polarization interferometry for measurement of surface profile. *Meas. Sens.* **2025**, *38*, 101827. [CrossRef]
9. Chen, K.H.; Wang, Y.H.; Chen, J.H.; Lin, C.H. Full-field refractive index measurement using absolute-phase total internal reflection heterodyne interferometry. *Appl. Phys. B-Lasers Opt.* **2020**, *126*, 109. [CrossRef]
10. Ma, H.; Liu, S.; Tao, T.; Chen, L.; Tang, L.; Li, C.; Wu, J.; Jia, X.; Wang, X.; Weng, J. A high-performance ranging method with a long distance range and high accuracy. *Optik* **2022**, *253*, 168526. [CrossRef]
11. Yi, L.; Jiang, Z.; Sun, A.; He, X.; Kong, Y.; Liu, C.; Wang, L. Rough surface profile measurement with spherical illuminating dual-wavelength shearing interferometry. *Opt. Commun.* **2026**, *602*, 132768. [CrossRef]
12. Yan, Y.; Veetil, S.P.; Zhu, P.; Gao, F.; Kong, Y.; He, X.; Sun, A.; Jiang, Z.; Liu, C. Compact Single-Shot Dual-Wavelength Interferometry for Large Object Measurement with Rough Surfaces. *Photonics* **2024**, *11*, 518. [CrossRef]
13. Kim, Y.; Hibino, K.; Kizaki, T.; Sugita, N.; Mitsuishi, M. Simultaneous interferometric measurement of the absolute thickness and surface shape of a transparent plate using wavelength tuning Fourier analysis and phase shifting. *Precis. Eng.* **2017**, *48*, 347–351. [CrossRef]
14. Guo, T.; Li, F.; Chen, J.; Fu, X.; Hu, X. Multi-wavelength phase-shifting interferometry for micro-structures measurement based on color image processing in white light interference. *Opt. Lasers Eng.* **2016**, *82*, 41–47. [CrossRef]
15. Arieli, Y.; Epshtein, S.; Yakubov, I.; Weitzman, Y.; Locketz, G.; Harris, A. Surface measurements by white light spatial-phase-shift imaging interferometry. *Opt. Express* **2014**, *22*, 15632–15638. [CrossRef]
16. Zhang, C.; Wang, G.; Gong, Z.; Lei, H.; Gong, P. Improving 3D measurement accuracy of fringe projection profilometry for complex textured objects by reducing projector-camera pixel matching errors. *Opt. Lasers Eng.* **2026**, *201*, 109661. [CrossRef]

17. Sanchez-Torres, M.; Hernández-Capuchin, I.; Ramírez-Fernández, C.; Clemente, E.; Sánchez-González, J.L.J.; López-Martínez, A. Recent Advances in Digital Fringe Projection Profilometry (2022–2025): Techniques, Applications, and Metrological Challenges—A Review. *Metrology* **2026**, *6*, 3. [CrossRef]
18. Xu, Y.; Jia, S.; Luo, X.; Yang, J.; Zhang, Y. Multi-frequency projected fringe profilometry for measuring objects with large depth discontinuities. *Opt. Commun.* **2013**, *288*, 27–30. [CrossRef]
19. Chen, Y.; He, Y.; Hu, E. Phase deviation analysis and phase retrieval for partial intensity saturation in phase-shifting projected fringe profilometry. *Opt. Commun.* **2008**, *281*, 3087–3090. [CrossRef]
20. Chang, W.Y.; Chen, K.H.; Chen, D.C.; Tseng, J.K.; Chen, S.T.; Sun, H.Y.; Chen, J.H.; Hsu, K.Y. Heterodyne moiré interferometry for measuring corneal surface profile. *Opt. Lasers Eng.* **2014**, *54*, 232–235. [CrossRef]
21. Chen, K.H.; Tsai, C.H.; Hung, S.C.; Chen, J.H. Surface profile measurement using heterodyne moiré signals with an adjustable grating period. *Appl. Opt.* **2026**, *65*, G10–G16. [CrossRef]
22. Dirckx, J.J.J.; Decraemer, W.F.; Dielis, G. Phase shift method based on object translation for full field automatic 3-D surface reconstruction from Moiré topograms. *Appl. Opt.* **1988**, *27*, 1164–1169. [CrossRef] [PubMed]
23. Quan, C.; Fu, Y.; Tay, C.J.; Tan, J.M. Profiling of objects with height steps by wavelet analysis of shadow moiré fringes. *Appl. Opt.* **2005**, *44*, 3284–3290. [CrossRef] [PubMed]
24. Chang, W.Y.; Hsu, F.H.; Chen, K.H.; Chen, J.H.; Hsu, K.Y. Heterodyne moiré surface profilometry. *Opt. Express* **2014**, *22*, 2845–2852. [CrossRef]
25. He, C.; Shen, Y.J.; Forbes, A. Towards higher-dimensional structured light. *Light Sci. Appl.* **2022**, *11*, 205. [CrossRef] [PubMed]
26. Cheng, M.J.; Jiang, W.J.; Guo, L.X.; Li, J.T.; Forbes, A. Metrology with a twist: Probing and sensing with vortex light. *Light Sci. Appl.* **2025**, *14*, 4. [CrossRef]
27. Zhang, Q.; He, Z.H.; Xie, Z.W.; Tan, Q.F.; Sheng, Y.L.; Jin, G.F.; Cao, L.C.; Yuan, X.C. Diffractive optical elements 75 years on: From micro-optics to metasurfaces. *Photonics Insights* **2023**, *2*, R09. [CrossRef]
28. Kozawa, Y.; Sato, S. Optical trapping of micrometer-size dielectric particles by cylindrical vector beams. *Opt. Express* **2010**, *18*, 10828–10833. [CrossRef]
29. Lan, T.H.; Chung, Y.K.; Li, J.E.; Tien, C.H. Plasmonic rainbow rings induced by white radial polarized. *Opt. Lett.* **2012**, *37*, 1205–1207. [CrossRef] [PubMed]
30. Rutkauskas, M.; Farrell, C.; Dorrer, C.; Marshall, K.L.; Lundquist, T.R.; Vedagarbha, P.; Reid, D.T. High-resolution subsurface microscopy of CMOS integrated circuits using radially polarized light. *Opt. Lett.* **2015**, *40*, 5502–5505. [CrossRef]
31. Meier, M.; Romano, V.; Feurer, T. Material processing with pulsed radially and azimuthally polarized laser radiation. *Appl. Phys. A* **2007**, *86*, 329–334. [CrossRef]
32. Zhan, Q. Cylindrical vector beam: From mathematical concepts to applications. *Adv. Opt. Photon.* **2009**, *1*, 1–57. [CrossRef]
33. Gilad, M.L.; Uriel, L. Radial polarization interferometer. *Opt. Express* **2009**, *17*, 23234–23246. [CrossRef] [PubMed]
34. Reza, S.A.; Imeri, A. Simultaneous thickness and phase index measurements with a motion-free actively tunable Twyman-Green. *Appl. Opt.* **2023**, *62*, 3948–3958. [CrossRef] [PubMed]
35. Kim, M.J.; Imeri, A.; Reza, S.A. Measuring the radius of curvature of spherical surfaces with actively tunable Fizeau and Twyman-Green interferometers. *Appl. Opt.* **2024**, *63*, 4077–4087. [CrossRef]

Disclaimer/Publisher's Note: The statements, opinions and data contained in all publications are solely those of the individual author(s) and contributor(s) and not of MDPI and/or the editor(s). MDPI and/or the editor(s) disclaim responsibility for any injury to people or property resulting from any ideas, methods, instructions or products referred to in the content.